Research Square

Preprints are preliminary reports that have not undergone peer review.
They should not be considered conclusive, used to inform clinical practice,
or referenced by the media as validated information.

Testing spatial Markovianity of breakthrough curves: a model-free criterion to discriminate heterogeneity-driven from mass-transfer- driven non-Fickian transport

Thi Thanh Hoa Nguyen

nthoa@hcmunre.edu.vn

Ho Chi Minh City University of Natural Resources and Environment (HCMUNRE)

Thi My Hong Tran

Ho Chi Minh City University of Technology (HCMUT)

Song Giang Le

Ho Chi Minh City University of Technology (HCMUT)

Research Article

Keywords: Non-Fickian transport, Breakthrough curves, Spatial Markov property, Mobile–immobile mass transfer, Model identifiability, Particle tracking

Posted Date: November 5th, 2026

DOI: https://doi.org/10.21203/rs.3.rs-11351053/v1

License: This work is licensed under a Creative Commons Attribution 4.0 International License.
Read Full License

Additional Declarations: No competing interests reported.

Testing spatial Markovianity of breakthrough curves: a model-free criterion to discriminate heterogeneity-driven from mass-transfer-driven non-Fickian transport

Thi Thanh Hoa Nguyen[1*], Thi My Hong Tran[2,3], Song Giang Le[2,3]

[1]Ho Chi Minh City University of Natural Resources and Environment (HCMUNRE), 236 Le Van Sy Street, Ho Chi Minh City, Vietnam

[2]Ho Chi Minh City University of Technology (HCMUT), 268 Ly Thuong Kiet Street, Ho Chi Minh City, Vietnam

[3]Vietnam National University – Ho Chi Minh City (VNU-HCM), Ho Chi Minh City, Vietnam

[*]Corresponding author. E-mail: ntthoa@hcmunre.edu.vn; ORCID: 0009-0008-2630-3794

Abstract

Non-Fickian breakthrough curves in porous media can be produced by spatially correlated velocity heterogeneity or by mass transfer to immobile regions, and a single breakthrough curve generally cannot tell these mechanisms apart. We show that a mobile–immobile model calibrated on the breakthrough curve of a strongly heterogeneous field ($\sigma^2_{\ln K} = 4$) at eight correlation lengths reproduces it over six orders of magnitude, yet mispredicts arrival-time densities by a factor of about two at 64 correlation lengths, while its fitted dispersivity and exchange rate drift with distance. We then exploit a property shared by all spatially Markovian transport models (advection–dispersion, mobile–immobile, multirate and uncorrelated continuous time random walk models): for flux-weighted injection, the breakthrough curve at distance $2d$ equals the self-convolution of the curve at d, so that all travel-time cumulants grow linearly with distance. Violations of this identity are a model-free signature of spatially variable transport. Using two-dimensional particle-tracking simulations, we construct a self-convolution test with controlled false-alarm rate and quantify its power for particle data and for noisy, censored concentration curves. We complement it with a flow-rate test based on the contraction of the scaled late-time tail expected when exchange is diffusion-controlled. Combined, the two tests classify heterogeneity-only, exchange-only and mixed regimes correctly in 86% of cases on average with 3000 samples per curve over a sweep of log-conductivity variance and capacity ratio. The results support the design of multi-distance, multi-rate tracer tests for mechanism identification.

Keywords: Non-Fickian transport, Breakthrough curves, Spatial Markov property, Mobile–immobile mass transfer, Model identifiability, Particle tracking

Article Highlights

- One tracer curve can look the same whether delays come from uneven flow paths or from solute trapped in stagnant zones
- Comparing curves at two distances reveals uneven flow paths without fitting any transport model
- Repeating the test at a lower flow rate reveals trapping, so both causes can be told apart in most cases

1 Introduction

Breakthrough curves (BTCs) measured in heterogeneous porous media are routinely non-Fickian: they show early arrivals, long late-time tails and spatial moments that do not grow linearly with travel distance (Gelhar et al. 1992; Berkowitz et al. 2006; Neuman and Tartakovsky 2009). Two physical mechanisms are usually invoked. The first is the heterogeneity of the advective velocity field, whose spatial correlation produces persistent fast and slow pathways (Dagan 1989; Le Borgne et al. 2008; Comolli et al. 2019). The second is mass transfer between mobile and immobile (or poorly connected) regions, in which solute is temporarily withdrawn from the flow by diffusion (Coats and Smith 1964; van Genuchten and Wierenga 1976; Haggerty and Gorelick 1995). Both mechanisms are present in most natural media, and experiments that visualise them directly show that they act jointly (Zinn et al. 2004; Gouze et al. 2008; Gjetvaj et al. 2015).

The macroscopic models used to interpret BTCs do not map one-to-one onto these mechanisms. The advection–dispersion equation (ADE), mobile–immobile (MIM) and multirate mass transfer (MRMT) models and the continuous time random walk (CTRW) are closely related: MRMT and CTRW are equivalent for a broad class of memory functions (Dentz and Berkowitz 2003), MIM is a special case of both, and upscaled heterogeneous advection can be represented by the same memory functions (Berkowitz et al. 2006; Willmann et al. 2008). A good fit of one of these models therefore says little about the mechanism. Different models can reproduce the same tail with different predictive skill (Pedretti and Bianchi 2018), and model selection can quantify whether data justify a model's complexity (Schöniger et al. 2015) but not which physical process is at work. The combined effect of both mechanisms has been analysed within a CTRW framework (Comolli et al. 2016), and non-Fickian signatures have been related to medium statistics (Bijeljic and Blunt 2006; Hansen et al. 2018; Pescimoro et al. 2022). The inverse question—which mechanism can be inferred from a limited set of observed BTCs, and with what confidence—has received less attention.

Measurements at several distances are an obvious source of additional information. Spatial Markov models (SMMs) describe particle transit times between equidistant control planes as a correlated Markov chain (Le Borgne et al. 2008; Kang et al. 2011, 2015) and have been extended to three-dimensional media and advective–diffusive transport (Cirpka et al. 2022; Stettler et al. 2026); Sherman et al. (2018) calibrated an inverse SMM on BTCs at two upstream ports of a column and improved the prediction at a downstream port compared with an uncorrelated CTRW. These studies use the spatial Markov structure to *model* transport; here we use it to *test* a hypothesis. If transport is spatially Markovian and stationary at the scale of the observation planes, the BTC at $2d$ must equal the self-convolution of the BTC at d, for any ADE, MIM, MRMT or uncorrelated CTRW model and any parameters, whereas correlated velocities and spatially non-stationary transport violate it. This yields a model-free criterion that requires no model calibration or comparison.

The objectives are to (i) show with controlled numerical experiments that a single BTC cannot discriminate heterogeneity from mass transfer even when the fit is excellent; (ii) derive two physically grounded signatures, the spatial Markov (self-convolution) property and the flow-rate scaling of the late-time tail; (iii) quantify the power and false-alarm rate of the corresponding tests for particle and noisy concentration data; and (iv) map the regimes in which heterogeneity, exchange or both can be identified.

2 Theory

2.1 Fine-scale transport model

We consider steady, incompressible Darcy flow in a heterogeneous, isotropic hydraulic conductivity field $K(\mathbf{x})$,

$$\nabla \cdot \mathbf{q} = 0, \qquad \mathbf{q} = -K(\mathbf{x})\nabla h, \tag{1}$$

and solute transport by advection with the pore velocity $\mathbf{v} = \mathbf{q}/\phi_m$ and molecular diffusion D_m in the mobile domain, coupled to first-order exchange with an unresolved (sub-grid) immobile domain (Coats and Smith 1964; van Genuchten and Wierenga 1976):

$$\frac{\partial c_m}{\partial t} + \nabla \cdot (\mathbf{v} c_m - D_m \nabla c_m) = -R\, k\, (c_m - c_{im}), \tag{2}$$

$$\frac{\partial c_{im}}{\partial t} = k\, (c_m - c_{im}), \tag{3}$$

where c_m and c_{im} are the mobile and immobile concentrations, $R = \phi_{im}/\phi_m$ is the capacity ratio and k the release rate (the mean residence time of a single immobile visit is $1/k$). For constant porosity, Eqs. (2)–(3) are equivalent to a Lagrangian description in which particles move by $\mathrm{d}\mathbf{X} =$

$\mathbf{v}(\mathbf{X})\,\mathrm{d}t + \sqrt{2D_m}\,\mathrm{d}\mathbf{W}$ while mobile, are trapped at rate Rk and are released at rate k (Delay et al. 2005; Salamon et al. 2006). Local mechanical dispersion is omitted, so that resolved heterogeneity is the only source of spreading besides diffusion; no drift correction is then required (LaBolle et al. 1996). We refer to three end-member mechanisms: (A) resolved heterogeneity without exchange ($R = 0$), (B) exchange in a homogeneous medium, and (C) heterogeneity combined with sub-grid exchange.

2.2 Breakthrough curves and the spatial Markov property

Particles are released on an injection plane $x = x_0$ with flux-weighted transverse positions. The breakthrough curve at distance d is the density $f_d(t)$ of the first-passage time $T(d)$ of particles through the plane $x = x_0 + d$, which corresponds to the flux-averaged concentration for a pulse injection (Kreft and Zuber 1978). We call transport *spatially Markovian and stationary* at scale d if two conditions hold: (i) Markov property—the motion after the first crossing of $x_0 + d$ depends on the past only through the particle state at that crossing; and (ii) stationarity—the state distribution at the crossing equals the injection distribution and the medium is statistically homogeneous along the mean flow, so that the transition law over $[x_0 + d, x_0 + 2d]$ equals that over $[x_0, x_0 + d]$. Together, (i) and (ii) make the sequence of segment travel times a renewal process; this is the null hypothesis tested below. The conditions hold for the ADE by the strong Markov property of Brownian motion with drift (Feller 1971), for the MIM model because particles cross a plane in the mobile state and trapping is memoryless, and for MRMT and uncorrelated CTRW models by construction (Dentz and Berkowitz 2003; Berkowitz et al. 2006).

Proposition 1 *If transport is spatially Markovian and stationary at scale d, then $T(2d) = T(d) + T'(d)$, where $T'(d)$ is independent of $T(d)$ and has the same distribution. Hence*

$$f_{2d} = f_d * f_d, \qquad \kappa_n(2d) = 2\,\kappa_n(d) \quad (n \geq 1), \tag{4}$$

where $*$ denotes convolution and κ_n the nth cumulant of T (for those n for which it exists). If the conditions hold at all scales, $\kappa_n(d) = c_n d$.

The proof follows from the strong Markov property at the first passage through $x_0 + d$, which makes the residual travel time independent of $T(d)$ (condition i), and from stationarity, which gives it the law of $T(d)$ (condition ii). A violation of Eq. (4) therefore has two possible sources: velocity memory (violating i) and spatial non-stationarity (violating ii). In a single realization of a heterogeneous medium, (ii) holds only in an ensemble sense; Sect. 4.7 separates the two contributions. Equation (4) contains no transport parameter, so a significant violation rejects the whole class of ADE, MIM, MRMT and uncorrelated CTRW models rather than a particular one. Flux-weighted injection is essential: it is the distribution with which particles cross any

downstream plane in a stationary flow (Dentz et al. 2016). For random walks with a fixed spatial step, d must be a multiple of the step; the identity also holds for heavy-tailed transit times whose cumulants do not exist. Correlated CTRWs and spatial Markov models violate it by construction.

In a heterogeneous field, the Lagrangian velocity of a particle is correlated over a distance of the order of the correlation length λ of $\ln K$ (Le Borgne et al. 2008; Dentz et al. 2016). Travel times over successive segments are then positively correlated, and

$$\kappa_2(2d) = 2\,\kappa_2(d) + 2\,\mathrm{Cov}[T(d),\, T(2d) - T(d)] > 2\,\kappa_2(d), \tag{5}$$

so that $\kappa_2(d)/d$ increases with d until $d \gg \lambda$. Adding sub-grid exchange to a heterogeneous field (mechanism C) adds to each segment a trapping delay that is conditionally independent between segments. It increases the variance of the increments but not their covariance, so it dilutes the correlation and shortens the distance over which the Markov property is violated.

2.3 Exact first-passage density of the mobile–immobile model

For one-dimensional transport with mobile velocity v, dispersion D and first-order exchange, $T(d) = T_m + \Theta$, where the mobile time T_m follows the inverse Gaussian density

$$g_d(u) = \frac{d}{\sqrt{4\pi D u^3}} \exp\left[-\frac{(d - vu)^2}{4Du}\right], \tag{6}$$

and, given T_m, the immobile time Θ is compound Poisson: $\mathcal{N} \sim \mathrm{Poisson}(RkT_m)$ visits of independent exponential durations with mean $1/k$. Hence

$$f_d(t) = e^{-Rkt} g_d(t) + \int_0^t g_d\,(u) \sqrt{\frac{Rk^2u}{t-u}}\; I_1\left(2k\sqrt{Ru(t-u)}\right) e^{-Rku - k(t-u)}\,\mathrm{d}u, \tag{7}$$

where I_1 is the modified Bessel function of the first kind; Eq. (7) was checked against numerical inversion of its Laplace transform (Sect. 3.4). We evaluate the integral by Gauss–Legendre quadrature in inverse-Gaussian quantile space, which is accurate for sharply peaked curves for which standard numerical Laplace inversion (Abate and Valkó 2004) becomes unreliable. The Laplace transform of Eq. (7), $\tilde{f}_d(s) = \exp\{d\left[v - \sqrt{v^2 + 4Dg(s)}\right]/(2D)\}$ with $g(s) = s + Rks/(s + k)$, makes the linearity of all cumulants in d explicit.

2.4 Flow-rate scaling

If the mean velocity is changed by a factor while the geometry is unchanged, advective travel times scale as $1/U$. Diffusion-controlled exchange, by contrast, has a rate k that does not depend on U. In the dimensionless time $\tau_U = tU/\lambda$, let $\tau_a = T_m U/\lambda$ denote the dimensionless mobile (advective) travel time of a particle. The number of immobile visits along its path is Poisson with mean $Rk\lambda\tau_a/U$ and each visit lasts on average $U/(k\lambda)$, so the scaled delay Θ_U has

$$\mathrm{E}[\Theta_U] = R\,\tau_a, \qquad \mathrm{Var}[\Theta_U] = \frac{2R\,\tau_a}{\mathrm{Da}}, \qquad \mathrm{Da} = \frac{k\lambda}{U}. \tag{8}$$

Lowering U increases the Damköhler number Da and contracts the late-time tail in scaled time, whereas pure advection through a fixed geometry gives scaled BTCs that collapse. For diffusion-controlled multirate exchange with capacities R_i and rates k_i, the variance becomes $\sum_i 2\,R_i\tau_a/\mathrm{Da}_i$ with $\mathrm{Da}_i = k_i\lambda/U$; every term decreases with U, but the late-time quantiles respond mainly to rates with Da_i of order one (Sect. 4.7). The argument requires an unchanged flow geometry. Diffusion into resolved low-conductivity inclusions is itself an exchange process; it acts in the same direction and limits the separation of "heterogeneity" and "exchange" (Sects. 4.6 and 5).

3 Numerical Methods

3.1 Fields, flow and particle tracking

Two-dimensional Gaussian $\ln K$ fields with exponential covariance and correlation length $\lambda = 1$ were generated by an FFT spectral method on a doubled periodic domain. The domain was $100\lambda \times 25\lambda$, discretised with square cells of size 0.2λ (500×125 cells). Flow (Eq. 1) was solved with a cell-centred finite-volume scheme (harmonic transmissibilities, fixed heads at inlet and outlet, no-flow lateral boundaries; maximum normalised cell divergence 7.9×10^{-10}), fluxes were rescaled to a mean pore velocity U, and velocities were interpolated linearly from face fluxes, which is divergence-free cell by cell (Pollock 1988).

Particles were tracked with an explicit random-walk scheme (Salamon et al. 2006) using an adaptive step $\Delta t = \min(c_a \Delta x/|\mathbf{v}|,\ 0.1\,\Delta x^2/D_m)$ with $c_a = 0.25$, reflecting lateral boundaries and $D_m = 0.01$ (Péclet number $\mathrm{Pe} = U\lambda/D_m = 100$ at $U = 1$). First passages through control planes at $d = 1,2,4,\ldots,64\lambda$ downstream of $x_0 = 5\lambda$ were recorded with linear interpolation within the step and a Brownian-bridge correction for crossings occurring between steps. Exchange was simulated by drawing exponential mobile durations with rate Rk and adding exponential immobile durations with rate k. Particles were injected over the central 21λ of the inlet plane, weighted by the normal flux (Fig. 1a). Mass recovery at the last plane was complete in all simulations.

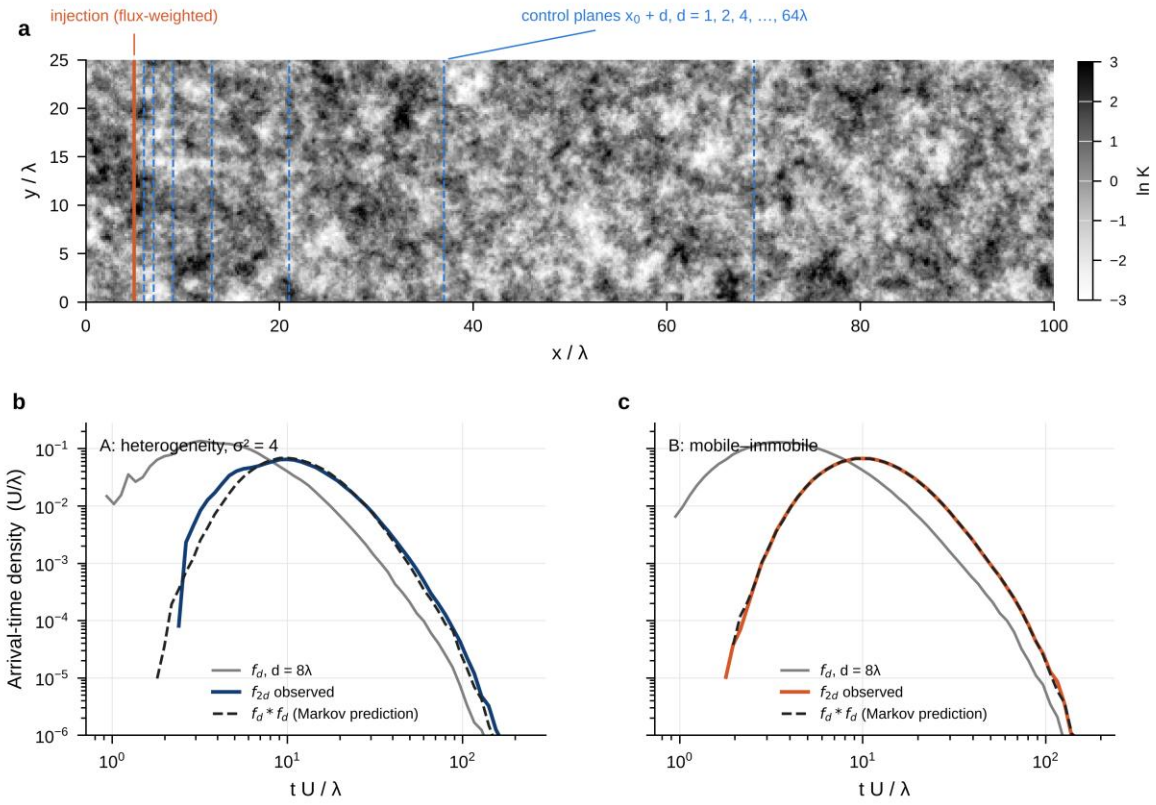


Fig. 1 Set-up and the self-convolution identity. **a** One realization of $\ln K$ ($\sigma^2_{\ln K} = 1$), flux-weighted injection plane and control planes. **b**, **c** Observed arrival-time density at 8λ (f_d), observed density at 16λ (f_{2d}) and the spatially Markovian prediction $f_d * f_d$ (dashed; self-convolution of the observed curve at 8λ, no model fitted) for mechanism A ($\sigma^2_{\ln K} = 4$) and mechanism B. Densities in units of U/λ, ensemble of 30 realizations

3.2 Numerical experiments

Mechanism A used $\sigma^2_{\ln K} \in \{0.5,1,2,4\}$ with 30 realizations of 20 000 particles each. Mechanism B was constructed to mimic A: we fitted a one-dimensional MIM model (Eq. 7) to the ensemble BTC of A ($\sigma^2_{\ln K} = 4$) at $d = 8\lambda$ by binned Poisson maximum likelihood on 60 logarithmic bins, obtaining $v = 1.083$, $D = 2.286$, $R = 0.071$ and $k = 0.078$, and sampled B exactly from Eq. (7) segment by segment; segment times are independent because the mobile motion restarts at each plane (strong Markov property) and trapping is memoryless. B is thus an *apparent* MIM, the worst-case mimic that a single-plane analysis of ergodic data would produce; a fit to one realization would inherit its particular preferential paths, which no homogeneous model can represent. Exchange-only media with parameters chosen independently of A are part of the classification sweep below. Mechanism C used the same 30 fields as A with $\sigma^2_{\ln K} = 1$ and added sub-grid exchange with $R = 0.5$, $k = 0.1$. Every simulation was repeated at $U = 1$ and $U = 0.25$ on the same fields and injection positions, with the exchange parameters of B and C (and the dispersivity $\alpha_L = (D - D_m)/v$ of B) kept fixed, as appropriate for diffusion-controlled exchange.

For the classification map, a sweep over $\sigma^2_{\ln K} \in \{0,0.5,1,2\}$ and $R \in \{0,0.1,0.3,1\}$ with $k = 0.1$ was run with 20 realizations of 20 000 particles at both flow rates, plus $k = 0.03$ and 0.3 at $(\sigma^2_{\ln K}, R) = (1,0.3)$. The very narrow BTCs of the homogeneous cells were computed with $c_a = 0.05$ to avoid a time-stepping artefact (Online Resource 1).

3.3 Statistical tests

All tests were applied to data from a single realization, as in an experiment, at significance level $\alpha = 0.05$, with rejection rates from 200 replicates unless stated otherwise. Each rate refers to one pre-selected plane pair; testing several pairs requires a multiple-testing correction.

Markov (self-convolution) test on particle data. From one realization, N arrival times at $2d$ and $2N$ arrival times at d were drawn from disjoint particle sets. The N pairwise sums of the latter sample $f_d * f_d$ under the null hypothesis, and a two-sample Kolmogorov–Smirnov test (Massey 1951) compared them with the observed times at $2d$ (the Anderson–Darling statistic was used as an alternative). To separate velocity memory from differences between the segments of one field, the test was also applied to ensemble samples, each arrival time drawn from an independently chosen realization. N, the number of independent tracer arrivals that make up a curve, measures its information content: for a measured curve with relative noise σ_r, Poisson counting gives the same relative error in the peak sampling interval when $N \approx 1/(\sigma_r^2 p_{\max})$, with $p_{\max}$ the mass fraction arriving in that interval. With 25 samples per median arrival time ($p_{\max} \approx 0.03$–0.04), $\sigma_r = 5\%$ and 10% correspond to $N \approx 10^4$ and 3×10^3.

Markov test on concentration data. To emulate measured BTCs, N arrival times per plane were binned on a sampling interval Δt of 1/25 of the median arrival time at d, normalised by the injected mass, perturbed by multiplicative Gaussian noise ($\sigma_r \in \{0,5,10\}\%$) and censored below a detection limit (DL) common to both planes (1% or 0.1% of the peak at d). The prediction at $2d$ is the discrete self-convolution of the curve at d, each pairwise sum split equally between adjacent bins to remove a half-interval bias. The statistic is the maximum difference between observed and predicted cumulative mass until 95% of the mass has arrived at $2d$, which avoids the censored tail. Its null distribution was obtained by a parametric bootstrap from the curve at d alone (Efron and Tibshirani 1993): Poisson counts per interval with means given by the measured curve and by its self-convolution were converted to concentrations, multiplied by the noise model and censored, in the same order as for the data (199 samples; 30 realizations per configuration). No transport model enters the test. Temporally autocorrelated (AR(1)) noise was also examined (Sect. 4.7).

Flow-rate (exchange) test. At $d = 16\lambda$, N arrival times at each flow rate were converted to scaled time tU. The statistic $\log\left(q_{95}^{U=1}/q_{95}^{U=0.25}\right)$, with q_{95} the 95th percentile, was compared with its

permutation distribution (Good 2005) (199 permutations) in a one-sided test for tail contraction at the lower flow rate, as predicted by Eq. (8).

Single-plane baselines. To quantify what one plane can reveal, we used (i) a two-sample Kolmogorov–Smirnov test between ergodic (pooled) samples of A and B at 8λ, and (ii) a goodness-of-fit test in which the MIM model was re-fitted to N arrival times of a single realization and assessed with a χ^2 statistic on logarithmic bins with at least five expected counts.

3.4 Verification

The generated fields had a variance of 1.008 for a target of 1, and a covariance at lag λ of 0.39 compared with $e^{-1} = 0.37$. In a homogeneous field, the simulated variance of $T(d)$ matched $2D_m d/U^3$ within 1.2% at $d = 2{,}10{,}40$. One-dimensional MIM walks reproduced Eq. (7) with mean arrival times within 0.5% of $d(1+R)/v$ and χ^2 per bin of 1.1–1.3; Eq. (7) and Talbot inversion of its Laplace transform (Abate and Valkó 2004) agreed to within 9×10^{-4} of the peak. Because particle tracking introduces no numerical dispersion, it cannot create artificial exchange-like tailing, which is essential for a study of mechanism identification.

4 Results

4.1 One plane is not enough to identify the mechanism

At the calibration plane the MIM model and the heterogeneous field are indistinguishable (Fig. 2b): the curves agree over six orders of magnitude, and a two-sample test between ergodic samples of A and B rejected at the false-alarm level (3–6.5%) for $N \leq 5000$ and in only 10.5% of cases at $N = 20\,000$. The calibrated model nevertheless fails at other distances (Fig. 2a,c,d): it misses the early arrivals carried by preferential paths and underestimates the late-time tail. The median absolute $\log_{10}$ error of the density grows from 0.020 at 8λ to 0.311 at 64λ (a factor of about two), and the 99th percentile at 64λ is 145 for A against 125 for B.

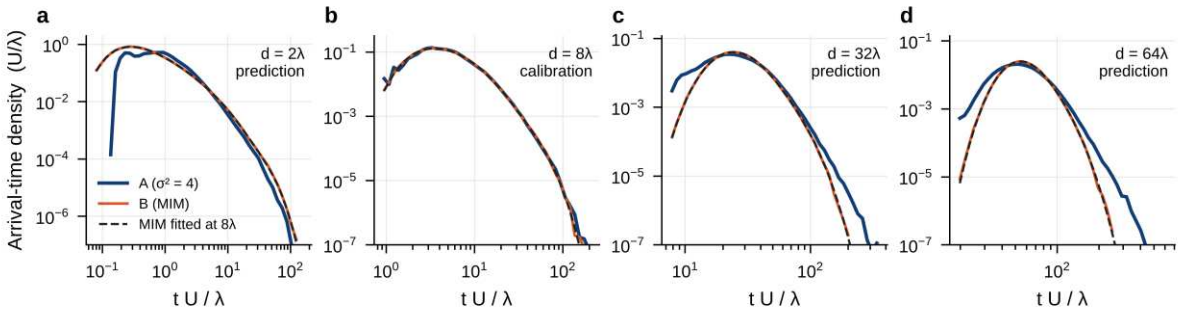


Fig. 2 Equifinality at one plane and failure of prediction. Arrival-time densities of A ($\sigma^2_{\ln K} = 4$, 30 realizations), B and the MIM model calibrated at 8λ, at **a** 2λ, **b** 8λ (calibration), **c** 32λ and **d** 64λ. Densities in units of U/λ

Re-fitting the MIM model independently at each plane reveals a systematic drift for A (Online Resource 1, Fig. S1): the apparent dispersivity grows from 0.66 to 3.9λ and the exchange rate decreases from 0.16 to 0.03 between $d = \lambda$ and 64λ, whereas the parameters of B remain constant within estimation noise. A scale-dependent apparent mass-transfer rate is widely reported in experiments (Haggerty et al. 2004); here it arises entirely from velocity correlation.

4.2 Distance signatures of spatially correlated velocities

Figure 1b,c illustrates Proposition 1: for B the self-convolution of the BTC at 8λ coincides with the BTC at 16λ, whereas for A it predicts too few early arrivals and too narrow a curve. The cumulants confirm this (Fig. 3). For B, $\kappa_2(d)/d$ is constant within 2%. For A it increases by a factor of 4.0–4.2 between $d = \lambda$ and 64λ for all variances, and $\kappa_3(d)/d$ by 11–16, so the Fickian regime is not reached at 64λ. The Spearman correlation between $T(d)$ and the increment $T(2d) - T(d)$ is 0.65–0.70 at $d = \lambda$, 0.20–0.25 at 8λ and -0.03 to 0.12 at 32λ, nearly independent of $\sigma^2_{\ln K}$, and vanishes for B ($|\rho_S| \leq 0.003$). At short separations, velocity memory rather than the strength of the heterogeneity therefore controls the violation.

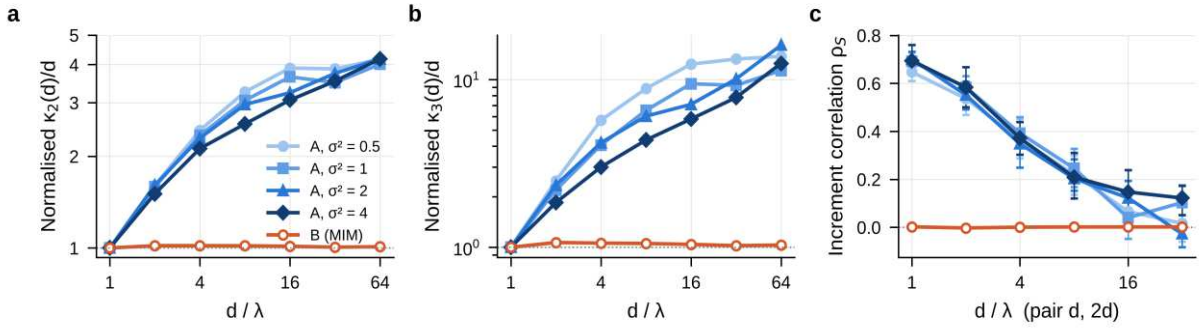


Fig. 3 Distance signatures. **a** Second and **b** third cumulant of the arrival time divided by distance, normalised by the value at $d = \lambda$; a spatially Markovian process gives a horizontal line at one. **c** Spearman correlation ρ_S between $T(d)$ and $T(2d) - T(d)$; bars are 95% bootstrap intervals over realizations

4.3 Power and false-alarm rate of the Markov test

The self-convolution test detects the heterogeneity of A ($\sigma^2_{\ln K} = 4$, planes 8λ and 16λ) with probability 0.30, 0.55, 0.85, 0.99 and 1.00 for $N = 100$, 300, 1000, 3000 and 5000 samples per curve, while its false-alarm rate for B stays at 2–7.5% for all plane pairs and N (Fig. 4a). With $N = 1000$ the power is 0.78–1.00 for plane pairs up to 8λ–16λ and 0.61–0.84 for pairs at 16–64λ, with no systematic dependence on $\sigma^2_{\ln K}$ (Fig. 4b); at the larger separations the rejections arise mainly from non-stationarity (Sect. 4.7).

A goodness-of-fit test of the MIM model re-fitted at a single plane also rejects A frequently (0.56, 0.88 and 0.96 for $N = 300$, 1000 and 3000; false-alarm rate 0.28 at $N = 300$ and 0.04 at larger N). This is not a contradiction of Sect. 4.1 but reflects a different objective. *Detecting the inadequacy of a particular model* is possible at one plane, because an individual realization departs from the smooth ensemble curve that B was built to match. *Identifying the mechanism* is not: at the ensemble level A and B give the same BTC, and any departure from one model can be absorbed by a more flexible spatially Markovian model (MRMT, CTRW). Identification needs a constraint on the whole class, which Proposition 1 supplies by relating two planes (see also Sect. 4.8).

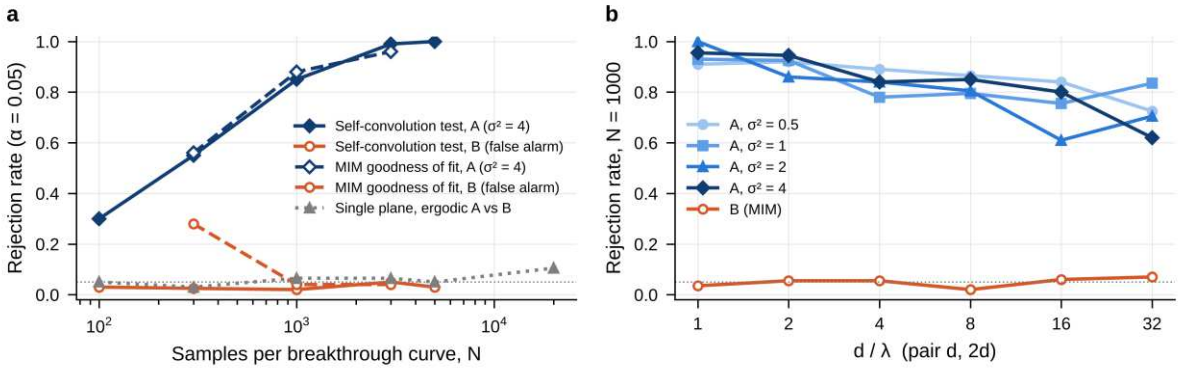


Fig. 4 Rejection rates of the tests applied to particle data from a single realization ($\alpha = 0.05$, dotted line). **a** Dependence on samples per BTC for the self-convolution test (8λ, 16λ), the single-plane goodness-of-fit test of a re-fitted MIM model and the single-plane comparison of ergodic A and B samples. **b** Self-convolution test with $N = 1000$ as a function of the plane pair

4.4 Heterogeneity combined with exchange, and the flow-rate signature

Mechanism C shares its fields and injection positions with A ($\sigma^2_{\ln K} = 1$), so their difference isolates the effect of exchange (Fig. 5), which dilutes the increment correlation (0.63 against 0.69 at $d = \lambda$, 0.14 against 0.25 at 8λ). The power of the Markov test with $N = 1000$ falls from 0.83 to 0.50 for the pair 8λ–16λ and from 0.79 to 0.17 for 32λ–64λ, and $\kappa_2(d)/d$ grows only by a factor of 1.3 between λ and 64λ instead of 4.0, as anticipated in Sect. 2.2. The mean arrival time at 64λ increases from 63.2 to 94.7, a ratio of $1.50 = 1 + R$ as required by mass balance.

The flow-rate signature behaves in the opposite way. When U is reduced from 1 to 0.25, the 99.9th percentile of the scaled arrival time contracts to 0.42–0.77 of its value for C, against 0.99–1.07 for A on the same fields (Fig. 5c). The contraction is weaker for B (0.71–0.85) because its capacity ratio is small, in agreement with Eq. (8). Without exchange, the ratio for A was 0.94–1.24 for $\sigma^2_{\ln K} \leq 2$ (above one at short distances, where diffusion broadens the scaled curve at lower Pe) and 0.86–0.95 for $\sigma^2_{\ln K} = 4$, where diffusion into low-conductivity inclusions acts as resolved exchange. The 90th percentile changed by less than 5%, so the signature resides in the late-time tail.

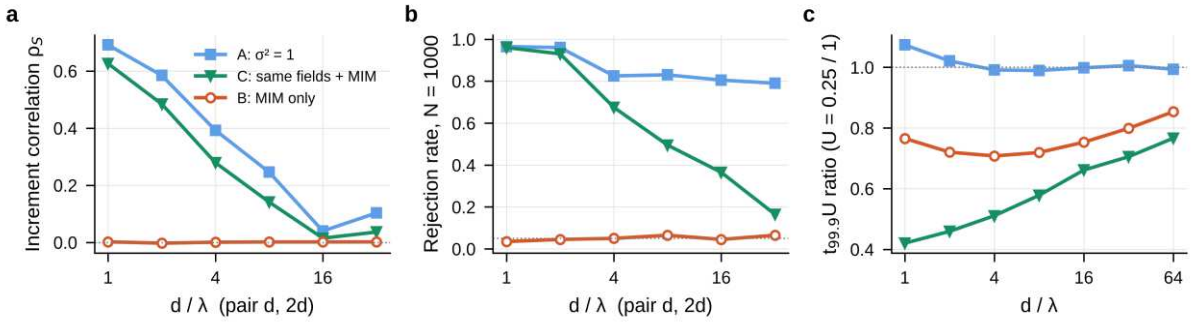


Fig. 5 Paired comparison of mechanism A ($\sigma^2_{\ln K} = 1$), mechanism C (same fields with $R = 0.5$, $k = 0.1$) and mechanism B. **a** Increment correlation. **b** Rejection rate of the self-convolution test ($N = 1000$). **c** Ratio of the 99.9th percentile of the scaled arrival time tU at $U = 0.25$ and $U = 1$

4.5 Concentration data with noise and detection limits

The bootstrap version of the Markov test retained its validity on emulated concentration data: across all noise levels, detection limits, N and plane pairs, it never rejected B (0 of 30 realizations per configuration). With 5% noise and a detection limit of 1% of the peak (planes 8λ, 16λ), it detected the heterogeneity of A ($\sigma^2_{\ln K} = 4$) in 23%, 60% and 80% of realizations for $N = 1000$, 3000 and 10^4 counts, of A ($\sigma^2_{\ln K} = 1$) in 7%, 40% and 67%, and of C in 3%, 10% and 37% (Fig. 6a). Increasing the noise to 10% reduced the power from 0.80 to 0.67 at $N = 10^4$, and lowering the detection limit to 0.1% had no systematic effect (Fig. 6b). Closer plane pairs gave higher power (Fig. 6c). The test is conservative (false-alarm rate near zero), so its power is below that of the particle-level test.

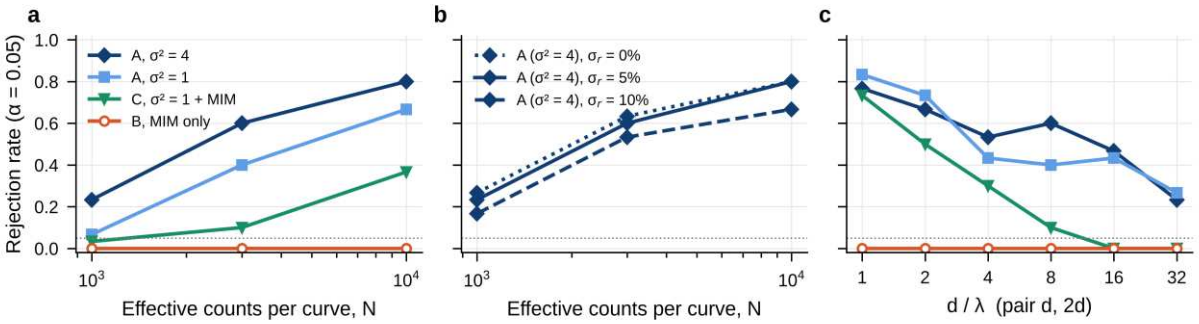


Fig. 6 Self-convolution test on emulated concentration BTCs with Poisson counting noise, multiplicative noise σ_r and a detection limit (DL). **a** Rejection rate against effective counts per curve, N, the number of tracer arrivals from which the curve is binned before noise is added (planes 8λ, 16λ; $\sigma_r = 5\%$, DL = 1%). **b** Effect of σ_r for A ($\sigma^2_{\ln K} = 4$). **c** Dependence on the plane pair ($N = 3000$). 30 realizations per point; dotted line: nominal level $\alpha = 0.05$

4.6 Classification of mechanisms

With control planes at 4λ and 8λ for the Markov test and two flow rates measured at 16λ for the exchange test, the combined classification was correct in 86% of replicates on average over the 16 cells of the $\sigma^2_{\ln K} \times R$ sweep for $N = 3000$, and in 70% for $N = 1000$ (Fig. 7, Table 1). False alarms of either test were controlled in the cells where the corresponding mechanism was absent: the Markov test rejected the homogeneous cells in 2.5–6% of replicates at $N = 3000$ (1.5–7.5% at $N = 1000$) and the exchange test never rejected a homogeneous field without exchange.

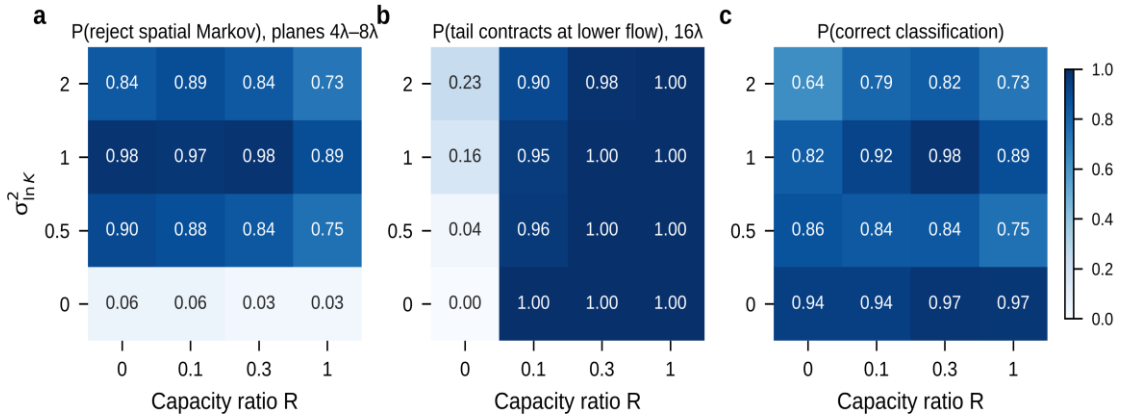


Fig. 7 Classification map over log-conductivity variance and capacity ratio ($k = 0.1$, $N = 3000$ samples per curve, 200 replicates per cell). **a** Rejection rate of the spatial Markov test (planes 4λ and 8λ). **b** Rejection rate of the flow-rate test for tail contraction (16λ). **c** Probability that the pair of test outcomes identifies the true regime (none, heterogeneity only, exchange only, both)

Table 1 Classification outcomes by true regime. Columns 3–6: fraction of replicates assigned to each regime at $N = 3000$ samples per curve (mean over the cells of the row; bold: correct). Last column: probability of correct classification at $N = 1000$ (range over cells). $k = 0.1$; 200 replicates per cell

True regime	$\sigma^2_{\ln K}$; R	None	Het.	Exch.	Both	Correct ($N = 1000$)
None	0; 0	**0.94**	0.06	0	0	0.93
Exchange only, weak	0; 0.1	0	0	**0.94**	0.06	0.83
Exchange only	0; 0.3, 1	0	0	**0.97**	0.03	0.97–0.99
Heterogeneity only	0.5, 1; 0	0.06	**0.85**	0.00	0.10	0.77–0.80
Heterogeneity only	2; 0	0.13	**0.64**	0.04	0.20	0.61
Both, weak exchange	0.5–2; 0.1	0.00	0.06	0.09	**0.85**	0.43–0.49
Both	0.5–2; 0.3	0	0.01	0.11	**0.88**	0.64–0.80
Both, strong exchange	0.5–2; 1	0	0	0.21	**0.79**	0.52–0.62

Two systematic confusions remain, both of physical origin (Table 1). First, strong exchange masks heterogeneity: at $R = 1$ the power of the Markov test dropped to 0.73–0.89 for the pair 4λ–8λ ($N = 3000$), so that mixed regimes were labelled exchange-only in 12–27% of replicates; the closer pair 2λ–4λ restored it to 0.94–0.97, which confirms the dilution mechanism of Sect. 2.2 and shows that the plane spacing should be adapted to the expected exchange capacity. Second, strong heterogeneity mimics exchange: for $\sigma^2_{\ln K} = 2$ without immobile zones the exchange test rejected in 14–24% of replicates (Sect. 5). The release rate had a moderate effect (0.97, 0.98 and 0.93 correct for $k = 0.03$, 0.1 and 0.3 at $\sigma^2_{\ln K} = 1$, $R = 0.3$). Weak exchange ($R = 0.1$) was the most difficult case at $N = 1000$ (0.43–0.49) and gained most from $N = 3000$ (0.79–0.92).

4.7 Robustness and sources of the Markov violation

Sensitivity analyses are detailed in Online Resource 1 (Table S1) and summarised here. *Memory versus non-stationarity.* At short separations the test rejects strongly for both single-realization and ensemble samples (A, $\sigma^2_{\ln K} = 1$, pair λ–2λ: 0.94 and 0.995), but at larger separations only for single-realization samples (8λ–16λ: 0.77 against 0.26; 32λ–64λ: 0.81 against 0.20). Velocity memory therefore explains the violation over a few correlation lengths, whereas further downstream it is dominated by differences between the two segments of a finite realization. Both are signatures of resolved heterogeneity: B was rejected in only 2.5–6% of cases in either mode. *Péclet number.* At Pe = 10, 100 and 1000 the increment correlation at $d = \lambda$ was 0.34, 0.67 and 0.72, and the single-realization power ($N = 1000$) 0.50–0.74, 0.72–0.99 and 0.81–1.00 (A, $\sigma^2_{\ln K} = 1$). *Statistic.* The Anderson–Darling statistic was more powerful than Kolmogorov–Smirnov (A, $\sigma^2_{\ln K} = 4$, 8λ–16λ: 0.91 against 0.85), with false alarms of 0.05–0.07, and is recommended for applications.

Quantile of the flow-rate test. The 90th percentile rarely detected weak exchange ($R = 0.1$: 0.00–0.22), and the 99th percentile detected it always but raised false alarms to 0.33 at $\sigma^2_{\ln K} = 2$, $R = 0$; the 95th percentile (0.92–1.00 and 0.25) is a compromise. *Exchange kinetics.* Single-rate

exchange in a homogeneous medium ($R = 0.3$, $N = 3000$) was detected in 98–100% of replicates for Da $= 0.03$–3 at $U = 1$, but never for Da ≤ 0.01: fewer than 5% of particles are then trapped at the higher flow rate, the 95th percentile does not reach them, and the scaled tail grows rather than contracts at lower U, although Eq. (8) still holds for the variance. With multirate exchange (Haggerty and Gorelick 1995), five rates between 0.03 and 3 were detected in 95% of replicates, but five rates between 0.003 and 3 only in 3%, because the responses of fast and slow rates cancel.

Autocorrelated noise. With AR(1) noise (coefficient 0.5 or 0.8, $\sigma_r = 5\%$, $N = 3000$) the concentration test rejected B in at most 1 of 30 realizations, whether or not the bootstrap reproduced the autocorrelation, and detected A ($\sigma^2_{\ln K} = 4$) in 50–63% of realizations, against 60% for uncorrelated noise.

4.8 Comparison with model-based approaches

Two model-based alternatives were applied to the same particle data ($N = 1000$ per plane, 25 replicates; Online Resource 1). *Single-plane model selection* (ADE versus MIM at 8λ, Akaike information criterion) inferred mass transfer in 72% of replicates for B, but also in 64% and 88% for A with $\sigma^2_{\ln K} = 1$ and 4, which contain no immobile zone: information criteria measure whether extra parameters are supported, not which process generated the tail (Schöniger et al. 2015). A *two-plane parameter-drift test*, in the spirit of calibrating upstream and predicting downstream (Sherman et al. 2018), compared a common MIM parameter set at 8λ and 16λ with separate sets (likelihood ratio, χ^2_4). It rejected B in 4% and A in 80–84% of replicates, comparable with the self-convolution test, but its null hypothesis is one model rather than a class: for a homogeneous, spatially Markovian medium with multirate exchange (five rates between 0.01 and 1, total capacity 0.3) it rejected in 44% of replicates, because the apparent single rate changes with distance, whereas the self-convolution test rejected in 6%. A spatial Markov model inverted from BTCs (Sherman et al. 2018) cannot identify its transition matrix from Eulerian BTCs without further assumptions; the self-convolution test is the part of its memory hypothesis that BTCs alone can test.

5 Discussion

What the two tests identify. The self-convolution test detects spatially variable transport: velocity memory over a few correlation lengths and, in a single field, differences between successive segments further downstream. A homogeneous medium with exchange passes it. The test does not measure how non-Fickian a BTC is—its power hardly depends on $\sigma^2_{\ln K}$—and passing it shows only that a spatially Markovian model with stationary transitions is adequate at the scale considered. Uncorrelated upscaled models (MRMT, CTRW) are therefore consistent with the data

beyond the memory length (Berkowitz et al. 2006; Comolli et al. 2019), whereas correlated models such as SMMs are required within it (Le Borgne et al. 2008; Kang et al. 2011; Cirpka et al. 2022); the test provides a data-based criterion for this choice, which has so far relied on comparing model predictions (Sherman et al. 2018). Tail contraction at lower flow rates is the signature of a rate-limited process whose time scale does not follow advection, and Eq. (8) states which feature of the BTC should respond and in which direction.

Limits of identifiability at high variance. For $\sigma^2_{\ln K} \geq 2$ the mechanisms cannot be separated cleanly: without immobile zones the flow-rate test rejected in 24% of replicates at $\sigma^2_{\ln K} = 2$ ($N = 3000$), and heterogeneity-only cases were classified correctly in only 64% (Table 1). Reducing the flow rate turns the slowest inclusions from advection- to diffusion-dominated: the area fraction with local Péclet number $|\mathbf{v}|\lambda/D_m < 1$ rose from 6×10^{-6} to 1.1×10^{-3} for $\sigma^2_{\ln K} = 2$ and from 1.0×10^{-3} to 1.5×10^{-2} for $\sigma^2_{\ln K} = 4$ when U was reduced from 1 to 0.25. Retention there is rate-limited exchange in the sense of Eq. (8): the flow-rate test identifies diffusion-controlled exchange whether it is resolved or sub-grid, the Markov test identifies resolved advective heterogeneity, and the label "both" for strongly heterogeneous fields is physically meaningful (Zinn et al. 2004; Gjetvaj et al. 2015; Comolli et al. 2016). The late-time slope of the BTC (Haggerty et al. 2004), a third flow rate and the magnitude of the contraction, which was weaker for resolved inclusions than for immobile zones with $R \geq 0.3$ (Sect. 4.4), can sharpen the distinction.

Applying the tests in practice. (i) *Unknown correlation length.* The particle-level power ($N = 1000$) remained between 0.6 and 1 for pairs between λ and 64λ (Fig. 4b), so misplaced planes do not remove it, but the concentration test and strong exchange favour closer pairs. Three or more planes in geometric progression ($d, 2d, 4d$), tested pairwise with a Holm correction, are preferable to a single pair; a $\ln K$ variogram, if available, fixes the scale. (ii) *Memory or non-stationarity.* With one realization, the dependence on separation is the diagnostic: memory causes rejections that weaken with separation, non-stationarity rejections at large separations that depend on the particular pair; repeated injections at different transverse positions provide a partial ensemble average. (iii) *Information content.* N reflects the noise level, not the number of samples: a curve with 5% relative noise and 3–4% of the mass in the peak interval corresponds to $N \approx 10^4$, and autocorrelated noise did not inflate false alarms. A few thousand effective counts are attainable in laboratory columns and high-precision tracer tests, but rarely with sparse field sampling; the bootstrap of Sect. 3.3 with the expected noise gives the achievable power in advance. (iv) *Flow-rate change.* The test requires the same flow geometry at both rates, as in columns and tanks with controlled pumping and, approximately, in forced-gradient tests at two pumping rates; under a

natural gradient, a flow interruption or tracers with different diffusion coefficients probe the same rate limitation. Very slow exchange falls outside the window of the 95th percentile (Sect. 4.7). (v) *Péclet number.* At $\mathrm{Pe} = 10$ transverse diffusion erases velocity memory within about one correlation length; at lower Pe the test mainly detects non-stationarity and needs closer planes or larger N.

Limitations. The study is two-dimensional, uses multi-Gaussian $\ln K$ fields and neglects local mechanical dispersion. In three dimensions streamlines can bypass inclusions in two transverse directions, which is expected to shorten the memory length, whereas connected high-conductivity structures (Zinn et al. 2004; Pescimoro et al. 2022) should prolong it. Systematic measurement errors such as baseline drift were not emulated. All conclusions are drawn from synthetic data; application to BTCs measured at several distances, such as multi-port column experiments (Sherman et al. 2018), is the necessary next step.

6 Conclusions

A single BTC can be reproduced equally well by mobile–immobile mass transfer and by correlated velocity heterogeneity, and the resulting model fails at other distances. The spatial Markov property—the BTC at $2d$ is the self-convolution of the BTC at d—holds for all ADE, MIM, MRMT and uncorrelated CTRW models, and its violation is a model-free signature of spatially variable transport: velocity memory at short separations and non-stationarity of the medium at larger ones. A test based on this identity had controlled false-alarm rates for particle and for noisy, censored concentration data, whereas an information criterion inferred mass transfer for most heterogeneity-only curves and a model-based drift test rejected a homogeneous multirate medium. Diffusion-controlled exchange leaves a flow-rate signature: the late-time tail contracts in scaled time when the flow rate is reduced, unless the exchange is so slow that few particles are trapped. Combined, the two tests distinguished heterogeneity-only, exchange-only and mixed regimes in most cases; for $\sigma^2_{\ln K} \geq 2$, diffusion into resolved low-conductivity regions is itself detected as exchange. The approach turns the choice of a macroscopic transport model into a testable hypothesis about the underlying physics.

Acknowledgements

To be added later

Declarations

Funding The authors did not receive support from any organization for the submitted work.

Competing interests The authors have no competing interests to declare that are relevant to the content of this article.

Author contributions Thi Thanh Hoa Nguyen: Conceptualization, Methodology, Software, Formal analysis, Writing – original draft. Thi My Hong Tran: Methodology, Validation, Writing – review and editing. Song Giang Le: Conceptualization, Supervision, Writing – review and editing. All authors read and approved the final manuscript.

Use of generative AI tools During the preparation of this work, the authors used DeepSeek to assist with literature searching, drafting, and language editing of the text. The authors reviewed and edited all content, verified all results, and take full responsibility for the content of the publication.

ORCID Thi Thanh Hoa Nguyen: https://orcid.org/0009-0008-2630-3794

Data availability The summary results underlying all figures and tables are included in Online Resource 2; the raw simulated arrival times (about 1 GB) can be regenerated with the code provided and are available from the corresponding author on reasonable request.

Code availability: The complete Python code for field generation, flow, particle tracking, the statistical tests and the figures, together with the summary result files, is provided to the editor and reviewers as Online Resource 2 and will be deposited in a public repository with a persistent identifier upon acceptance.

References

Abate J, Valkó PP (2004) Multi-precision Laplace transform inversion. International Journal for Numerical Methods in Engineering 60:979–993. https://doi.org/10.1002/nme.995

Berkowitz B, Cortis A, Dentz M, Scher H (2006) Modeling non-Fickian transport in geological formations as a continuous time random walk. Reviews of Geophysics 44:RG2003. https://doi.org/10.1029/2005RG000178

Bijeljic B, Blunt MJ (2006) Pore-scale modeling and continuous time random walk analysis of dispersion in porous media. Water Resources Research 42:W01202. https://doi.org/10.1029/2005WR004578

Cirpka OA, Stettler M, Dentz M (2022) Spatial Markov model for the prediction of travel-time-based solute dispersion in three-dimensional heterogeneous media. Water Resources Research 58:e2022WR032215. https://doi.org/10.1029/2022WR032215

Coats KH, Smith BD (1964) Dead-end pore volume and dispersion in porous media. Society of Petroleum Engineers Journal 4:73–84. https://doi.org/10.2118/647-PA

Comolli A, Hakoun V, Dentz M (2019) Mechanisms, upscaling, and prediction of anomalous dispersion in heterogeneous porous media. Water Resources Research 55:8197–8222. https://doi.org/10.1029/2019WR024919

Comolli A, Hidalgo JJ, Moussey C, Dentz M (2016) Non-Fickian transport under heterogeneous advection and mobile-immobile mass transfer. Transport in Porous Media 115:265–289. https://doi.org/10.1007/s11242-016-0727-6

Dagan G (1989) Flow and transport in porous formations. Springer, Berlin

Delay F, Ackerer P, Danquigny C (2005) Simulating solute transport in porous or fractured formations using random walk particle tracking: A review. Vadose Zone Journal 4:360–379. https://doi.org/10.2136/vzj2004.0125

Dentz M, Berkowitz B (2003) Transport behavior of a passive solute in continuous time random walks and multirate mass transfer. Water Resources Research 39:1111. https://doi.org/10.1029/2001WR001163

Dentz M, Kang PK, Comolli A, et al (2016) Continuous time random walks for the evolution of Lagrangian velocities. Physical Review Fluids 1:074004. https://doi.org/10.1103/PhysRevFluids.1.074004

Efron B, Tibshirani RJ (1993) An introduction to the bootstrap. Chapman & Hall, New York

Feller W (1971) An introduction to probability theory and its applications, vol. II, 2nd edn. Wiley, New York

Gelhar LW, Welty C, Rehfeldt KR (1992) A critical review of data on field-scale dispersion in aquifers. Water Resources Research 28:1955–1974. https://doi.org/10.1029/92WR00607

Gjetvaj F, Russian A, Gouze P, Dentz M (2015) Dual control of flow field heterogeneity and immobile porosity on non-Fickian transport in Berea sandstone. Water Resources Research 51:8273–8293. https://doi.org/10.1002/2015WR017645

Good PI (2005) Permutation, parametric, and bootstrap tests of hypotheses, 3rd edn. Springer, New York

Gouze P, Melean Y, Le Borgne T, et al (2008) Non-Fickian dispersion in porous media explained by heterogeneous microscale matrix diffusion. Water Resources Research 44: https://doi.org/10.1029/2007WR006690

Haggerty R, Gorelick SM (1995) Multiple-rate mass transfer for modeling diffusion and surface reactions in media with pore-scale heterogeneity. Water Resources Research 31:2383–2400. https://doi.org/10.1029/95WR10583

Haggerty R, Harvey CF, Freiherr von Schwerin C, Meigs LC (2004) What controls the apparent timescale of solute mass transfer in aquifers and soils? A comparison of experimental results. Water Resources Research 40:W01510. https://doi.org/10.1029/2002WR001716

Hansen SK, Haslauer CP, Cirpka OA, Vesselinov VV (2018) Direct breakthrough curve prediction from statistics of heterogeneous conductivity fields. Water Resources Research 54:271–285. https://doi.org/10.1002/2017WR020450

Kang PK, Dentz M, Le Borgne T, Juanes R (2011) Spatial Markov model of anomalous transport through random lattice networks. Physical Review Letters 107:180602. https://doi.org/10.1103/PhysRevLett.107.180602

Kang PK, Le Borgne T, Dentz M, et al (2015) Impact of velocity correlation and distribution on transport in fractured media: Field evidence and theoretical model. Water Resources Research 51:940–959. https://doi.org/10.1002/2014WR015799

Kreft A, Zuber A (1978) On the physical meaning of the dispersion equation and its solutions for different initial and boundary conditions. Chemical Engineering Science 33:1471–1480. https://doi.org/10.1016/0009-2509(78)85196-3

LaBolle EM, Fogg GE, Tompson AFB (1996) Random-walk simulation of transport in heterogeneous porous media: Local mass-conservation problem and implementation methods. Water Resources Research 32:583–593. https://doi.org/10.1029/95WR03528

Le Borgne T, Dentz M, Carrera J (2008) Lagrangian statistical model for transport in highly heterogeneous velocity fields. Physical Review Letters 101:090601. https://doi.org/10.1103/PhysRevLett.101.090601

Massey FJ (1951) The Kolmogorov-Smirnov test for goodness of fit. Journal of the American Statistical Association 46:68–78. https://doi.org/10.1080/01621459.1951.10500769

Neuman SP, Tartakovsky DM (2009) Perspective on theories of non-Fickian transport in heterogeneous media. Advances in Water Resources 32:670–680. https://doi.org/10.1016/j.advwatres.2008.08.005

Pedretti D, Bianchi M (2018) Reproducing tailing in breakthrough curves: Are statistical models equally representative and predictive? Advances in Water Resources 113:236–248. https://doi.org/10.1016/j.advwatres.2018.01.023

Pescimoro E, Icardi M, Porta G, Bianchi M (2022) Emergence of non-Fickian transport in truncated pluri-Gaussian permeability fields. GEM – International Journal on Geomathematics 13:17. https://doi.org/10.1007/s13137-022-00207-4

Pollock DW (1988) Semianalytical computation of path lines for finite-difference models. Groundwater 26:743–750. https://doi.org/10.1111/j.1745-6584.1988.tb00425.x

Salamon P, Fernàndez-Garcia D, Gómez-Hernández JJ (2006) A review and numerical assessment of the random walk particle tracking method. Journal of Contaminant Hydrology 87:277–305. https://doi.org/10.1016/j.jconhyd.2006.05.005

Schöniger A, Illman WA, Wöhling T, Nowak W (2015) Finding the right balance between groundwater model complexity and experimental effort via Bayesian model selection. Journal of Hydrology 531:96–110. https://doi.org/10.1016/j.jhydrol.2015.07.047

Sherman T, Foster A, Bolster D, Singha K (2018) Predicting downstream concentration histories from upstream data in column experiments. Water Resources Research 54:9684–9694. https://doi.org/10.1029/2018WR023420

Stettler M, Dentz M, Cirpka OA (2026) Spatial Markov model of advective-diffusive transport in heterogeneous domains. Water Resources Research 62:e2025WR041175. https://doi.org/10.1029/2025WR041175

van Genuchten MTh, Wierenga PJ (1976) Mass transfer studies in sorbing porous media I. Analytical solutions. Soil Science Society of America Journal 40:473–480. https://doi.org/10.2136/sssaj1976.03615995004000040011x

Willmann M, Carrera J, Sánchez-Vila X (2008) Transport upscaling in heterogeneous aquifers: What physical parameters control memory functions? Water Resources Research 44:W12437. https://doi.org/10.1029/2007WR006531

Zinn B, Meigs LC, Harvey CF, et al (2004) Experimental visualization of solute transport and mass transfer processes in two-dimensional conductivity fields with connected regions of high conductivity. Environmental Science & Technology 38:3916–3926. https://doi.org/10.1021/es034958g

Supplementary Files

This is a list of supplementary files associated with this preprint. Click to download.

- OnlineResource1.pdf
- OnlineResource2codeandresults.zip